Optically Transparent Holographic Display Antenna: High Gain, Beam Steering, and Lossless Bonding for 5G Millimeter-Wave n261 Band

BYEONGJIN KIM [1] **(Graduate Student Member, IEEE), SUK HWANGBO** [2] **(Member, IEEE), AND JUNGSUEK OH** [1] **(Senior Member, IEEE)**

[1] Institute of New Media and Communications, Department of Electrical and Computer Engineering, Seoul National University, Seoul 08826, South Korea
[2] Wireless Semiconductor Division, Broadcom, Seoul 06771, South Korea

CORRESPONDING AUTHOR: J. OH (e-mail: jungsuek@snu.ac.kr)

ABSTRACT This paper presents a novel high-gain beam-forming holographic display antenna (HDA) concept that utilizes surface waves on the wide display area of 5G millimeter-wave (mmWave) devices. The HDA consists of two components: a 1×4 surface wave launcher array (SWLA) that excites phased surface waves on the display cover glass, and an optically transparent holographic metasurface that transforms surface waves into radiating waves. Therefore, the proposed HDA is free from the radiation pattern distortion issues reported for conventional display antennas. The surface-wave-based HDA can sustain efficient radiation performance even when the metal pattern area within each unit cell of the holographic metasurface is significantly reduced–unlike conventional transmission-line-based display antennas, whose performance degrades as the metal area is minimized to improve optical transparency. A single-ring-type optically transparent holographic metasurface unit cell was found to exhibit a wide surface reactance range despite having a super-thin linewidth and thickness. Furthermore, the proposed SWLA has a compact form factor to be embedded within a thin display bezel area. It is designed with a unique component-separated structure that eliminates the detrimental bonding loss that occurs in conventional display antennas. Finally, its unique array spacing condition for higher taper efficiency is determined. Measured results show that the HDA exhibits a high gain of 14.2 dBi and a -3 dB beam scan range of 68° $(-34°-34°)$. The proposed HDA covers the n261 band (27.5−28.35 GHz), while the -3 dB gain bandwidth also covers the n257 band (26.5-29.5 GHz).

INDEX TERMS Holographic metasurface, optically transparent, beam steering, display antenna, holographic display antenna, 5G, 5G millimeter-wave (MmWave).

I. INTRODUCTION

WITH the commercialization of 5G millimeter-wave (mmWave) communication networks and devices such as smartphones, numerous antenna solutions such as antenna-in-package (AiP) [1], [2], [3], [4], [5], [6], [7], [8], [9], antenna-on-chip (AoC) [10], [11], [12], antenna-on-package (AoP) [13], [14], [15], antenna-on-display (AoD) [16], [17], [18], [19], [20], [21], [22], [23], [24], and antenna-in-display (AiD) [25], [26] have been proposed to overcome the high interconnection and transmission losses caused by the use of high frequency bands. For example,

most 5G mmWave smartphones have adopted a method by which one to three AiPs can be compactly incorporated into the edge of the mainboard on the rear. There is not enough space for antennas on the rear mainboard because of the numerous other components such as cameras, batteries, USB ports, sensors, and various low-frequency antennas and circuits; therefore, the display antenna concept has emerged in which the antennas are embedded into the display by mounting them on the display cover glass or at the edge of the OLED [16], [17], [18], [19], [20], [21], [22], [23], [24], [25], [26].

In the case of AoD, transparent conductors such those using ITO-based metals and metal meshes [27], [28], [29], [30], [31], [32], [33], [34], [35], [36] are used to avoid obstructing the display visibility. Resonant-type transmission line-based AoDs typically suffer from low radiation efficiency and gain owing to the high resistivity of transparent conductors and the use of OLED as a ground, which are imperfect conductors [16], [17], [18], [19], [20], [21], [22], [23]. Although there has been a report on AoD using surface waves [24], endfire radiation requires modifications to be made to the metal frames of smartphones [37], making immediate adoption challenging. Furthermore, the addition of an antenna substrate and adhesive films to the AoD design increases the display thickness, which is unattractive to the industry. Additionally, anisotropic conductive film (ACF) bonding between the antenna film and flexible printed circuit board (FPCB) causes a detrimental bonding loss of up to 4 dB, resulting in low gain and low radiation efficiency [16].

In AiD, the antenna radiators are placed in a very thin dead space at the edge of the OLED screen [25], [26]. As a transparent conductor design is not required, the radiation efficiency and gain can be high. However, relocating the driving circuits for the OLED and touch sensor panels, originally located in dead space is challenging, which can lead to an increased OLED area and significantly higher manufacturing costs. Additionally, because of the spurious radiation from undesired surface waves excited on the large display area, both AoD and AiD suffer from beam distortion issues, such as a beam pattern with undesired fluctuations and beam tilt toward the display direction [20].

Recently, holographic metasurface antennas (HMAs) that utilize surface waves propagating on a grounded dielectric slab for radiation have been studied in the high-frequency bands [38], [39], [40], [41], [42], [43], [44]. In a periodic leaky wave antenna, HMA uses the surface wave as a reference wave and analytically matches the surface reactance of periodic metal patterns to create the desired radiated wave. An antenna that feeds a surface wave is called a surface wave launcher (SWL), and there are various types of SWLs, such as monopole and substrate integrated waveguide (SIW) horn, probe-fed reflector, circular patch, annular slot, slot, and vivaldi-type [38], [39], [40], [41], [42], [43], [44], [45], [46], [47], [48], [49], [50]. While primary radiating elements, such as slots, are typically designed to have a lateral size which is approximately half a wavelength, previous studies often required either quarter-wavelength-tall vertical structures [39], [40], [41], [45] or additional components, such as large matching stubs [42], [43], [44], [46], [47], [48], [49], [50], to achieve efficient excitation. As a result, the overall form factors of these SWLs are often too bulky for practical integration into compact electronic systems, such as smartphones.

Meanwhile, there have been a few designs of HMAs which are capable of fixed-frequency beam steering, which is essential for 5G mmWave applications where beamforming is essential [51], [52]. In [51], 1-bit phase tuning was utilized

for each of the four SWL elements. In [52], an HMA with a two-element (1×2) SWL array (SWLA) achieving a maximal scan angle of 18° was measured, and an HMA with a 1×6 SWLA was simulated. For the former, the gain and scan range were limited to less than 10 dBi and 6°, respectively. For the latter, continuous beam-scanned patterns were not observed and only normalized beam patterns are shown, without presenting an absolute gain. Additionally, HMAs to be used as display antennas, they must be optically transparent. ITO has also been used in [53]. However, because ITO has low conductivity, a metal mesh is often used in the design of display antennas to improve radiation efficiency [16], [17], [18], [19], [20], [21], [22], [23], [24].

In this paper, we propose a new type of display antenna, the holographic display antenna (HDA), which operates in the n261 band and effectively controls the surface waves excited over a large display area to achieve high-gain beamforming without beam distortion. Transmission-line-based display antennas, such as AoD and AiD, suffer from increased transmission-line resistance as the metal area is reduced to enhance optical transparency (OT). As a result, it is challenging to effectively utilize the entire aperture area for radiation purposes, especially on electrically large surfaces such as displays. In contrast, because surface waves inherently propagate well along a grounded dielectric slab (GDS), even without metal on its surface [54], the surface-wave-based HDA can sustain an efficient radiation performance even when the metal pattern area in each unit cell of the holographic metasurface is significantly reduced. The novelties compared with existing display antennas are as follows:

1) Conventional display antennas suffer from beam pattern distortion caused by surface waves excited over a large display area. However, by incorporating holographic metasurface technology for the first time, HDA controls and utilizes surface waves for radiation, enabling high peak gain in the desired direction without beam tilt or undesired fluctuations in the radiation pattern.

2) The unique component-separated structure of SWLA eliminates the detrimental bonding loss observed in conventional display antennas. Moreover, because of the compact placement of the SWLA in the thin display bezel at the bottom edge of the front glass–bezel refers to the border area surrounding the active display region [25]–a transparent design for the SWLA is not required. This enables a high radiation efficiency. Additionally, by placing an optically transparent ground at the bottom of the front glass, stable performance can be achieved without using the OLED, which is an imperfect conductor, as the ground.

3) An optically transparent holographic metasurface unit cell in hybrid form, combining a fine-metal single-ring and a metal-mesh ground, is designed to demonstrate
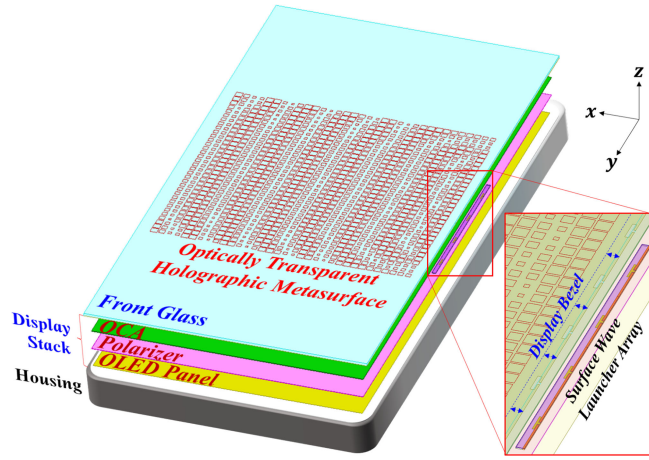
FIGURE 1. Conceptual illustration of an optically transparent holographic display antenna (HDA) integrated into a 5G millimeter-wave (mmWave) smartphone. The HDA consists of a transparent holographic metasurface on the display cover glass and a non-transparent SWLA embedded in the bezel area.

FIGURE 2. Illustrations of (a) the surface wave launcher array (SWLA) embedded in the display bezel area and (b) the SWLA element.

the feasibility of a stable HDA design despite its super-thin linewidth and thickness.

4) A 1×4 SWLA-fed high-gain beamforming HMA applicable to 5G mmWave cellular devices has been designed and measured for the first time.

This paper is structured as follows: Section II discusses the configuration of the HDA and a compact surface wave launcher that can be embedded in a thin display bezel. The operational principle and design procedure of the HMA are explained in Section III. Section IV describes the characteristics of transparent holographic metasurface unit cells. In Section V, we discuss the HDA design process and analyze its gain and beamforming characteristics. Section VI presents fabrication and measurements. Finally, Section VII concludes the paper.

II. INTEGRATION OF HOLOGRAPHIC METASURFACE AND SWLA IN A DISPLAY FOR 5G MMWAVE DEVICES

A. CONFIGURATION OF THE HOLOGRAPHIC DISPLAY ANTENNA

Fig. 1 provides an overview of the proposed HDA concept, illustrating its key components: an optically transparent holographic metasurface printed on both the top and bottom surfaces of the display cover glass, and a non-transparent SWLA embedded in the display bezel area. The detailed configurations of these components are shown in Fig. 2. The Samsung Galaxy 24 smartphone model is exemplified as a recent 5G mmWave smartphone, and its 147.0 mm×70.6 mm display-cover-glass covers other display layers such as a polarizer, optically clear adhesive (OCA), and OLED [25], with a 1.5 mm wide margin, which is referred to as the display bezel area. Notably, the holographic metasurface and SWLA share the ground printed on the bottom of the cover glass. The configurations of the display layers and bezel area illustrated in more detail in Fig. 2. The optically transparent mesh ground under the holographic metasurface is connected to a nontransparent
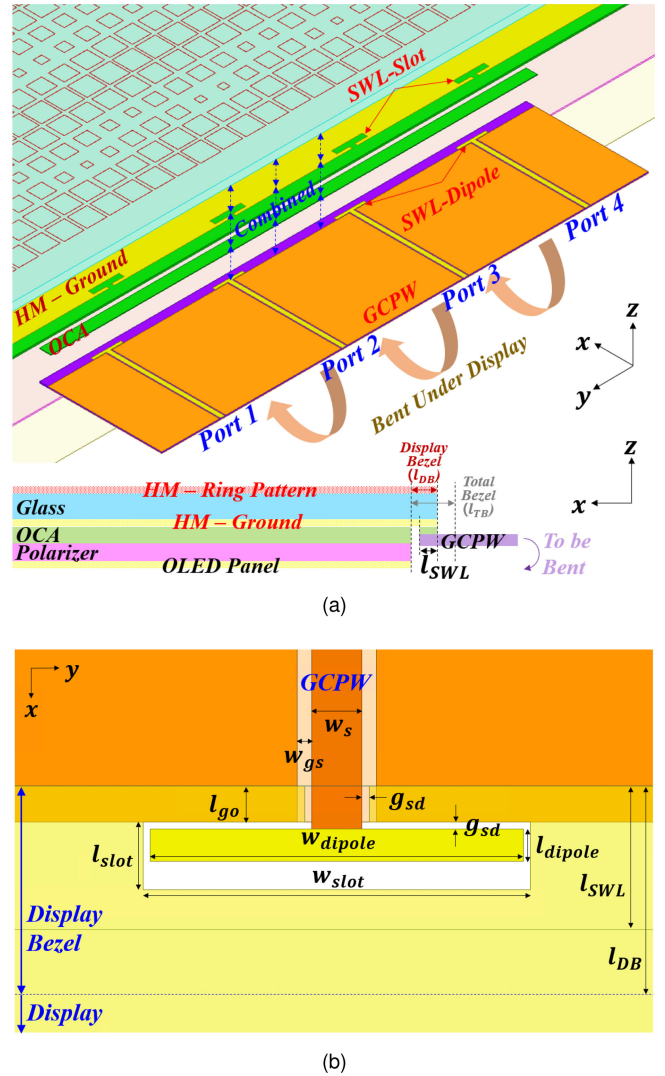
ground that is coplanar with the SWLA. The thicknesses of the glass, polarizer, OCA between the holographic meta-surface (HM) and polarizer, and the OCA between the HM and GCPW are 0.7 mm, 0.104 mm, 0.15 mm, and 0.05 mm, respectively. The dielectric constants of the glass, polarizer, and OCA were 5.27, 2.92, and 2.58, respectively. Eagle XG glass was selected as the glass material, and information on the polarizer and OCA was obtained from [25].

Fig. 2(a) shows an enlarged view of the SWLA, revealing that the proposed SWL consists of two closely stacked parts: one is a slot defected in the ground printed on the bottom of the cover glass and the other is a center-fed dipole printed on a grounded coplanar waveguide (GCPW) formed on a separate flexible printed circuit board (FPCB).

Notably, a Taconic-TLY substrate, which has a similar dielectric constant and loss tangent to polyimide (PI) films typically used for FPCBs, was used as the substrate for the GCPW instead of a PI film for ease of fabrication and

TABLE 1. Optimized dimensions (in mm) and design parameter values.

Parameter	Value	Parameter	Value	Parameter	Value
w_s	0.35	l_{slot}	0.475	l_w	0.01
w_{gs}	0.1	l_{TB}	2.5	g_{SH}	2.225
g_{sd}	0.05	l_{DB}	1.5	D_x	69
l_{go}	0.25	l_{SWL}	1	D_y	68
w_{dipole}	2.6	a	2	d	10.7
w_{slot}	2.7	$D_{g,mesh}$	0.4	t	0.0006
l_{dipole}	0.225	h	0.7	ϕ_{offset}	π

TABLE 2. Lateral and vertical sizes of conventional and proposed SWL element.

Ref.	Lateral Size ($*\lambda_0 \times \lambda_0$)	Vertical Size (λ_0)
[39]	0.56×0.56	0.08
[40]	N/A	0.25
[41]	N/A	0.25
[42]	$**3.42 \times 1.89$	0.12
[43]	$**0.16 \times 0.13$	0.082
[44]	1.38×0.58 & $**0.40 \times 0.38$	0.091
[45]	N/A	0.25
[46]	1.16×0.71	0.12
[47]	2.46×1.38	0.23
[48]	$**0.86 \times 0.86$	0.08
[49]	0.27×0.27	0.10
[50]	$**0.27 \times 0.20$	0.10
This work	0.25×0.068	0.065

* λ_0 denotes the free-space wavelength at the center frequency.
** Estimated from the figure based on available dimension data and proportional scaling, as some dimension values were not explicitly provided.

measurement. In a real use case, the FPCB is bent under the OLED panel and connected to a driving radiofrequency integrated circuit (RFIC) placed on the mainboard, similar to previous AoD and AiD designs [16], [25]. Space for the transmission lines of the display antennas to be bent has already been provided in 5G mmWave cellular devices because of the empty volume inside the smartphone housing under the wide total bezel area. For instance, the example smartphone model has a 1.5 mm wide display bezel and a 2.5 mm wide total bezel area. The optimized dimensions (in mm) and design parameters of the proposed HDA are listed in Table 1.

While the proposed HDA is vertically aligned above the wireless charging coil, potential electromagnetic interference is effectively minimized due to the significant frequency separation between the two systems (28 GHz compared to 100–300 kHz). In addition, intermediate layers commonly present in display stacks–such as the OLED backplane and ferrite shielding–further reduce low-frequency magnetic field coupling, thus preserving the performance of the HDA.

B. NOVELTY IN THE SWLA DESIGN
The proposed SWLA design introduces three key innovations: compact lateral and vertical dimensions, elimination of ACF bonding loss, and an unprecedented 1λ array spacing.

First, the proposed SWL element features compact lateral and vertical dimensions, which are essential for integration into modern electronic devices requiring ultra-thin profiles and highly condensed component arrangements. Table 2 summarizes a comparison of the physical dimensions of the proposed and conventional SWL implementations. Monopole-type SWLs with a height of 0.25λ are impractical for display antenna applications because of their excessive vertical profiles. Compared to other non-monopole-type SWLs, the proposed design achieves the smallest footprint in both the lateral and vertical dimensions, making it the only viable option for integration into the proposed HDA, where the available space is strictly limited to the narrow display bezel region.

Second, the component-separated architecture of the SWLA eliminates the detrimental bonding loss typically observed in conventional display antennas such as AoDs and AiDs [16], [17], [18], [19], [20], [21], [22], [23], [24], [25]. In those architectures, the antenna elements are directly bonded to the feeding network on the FPCB using

ACF, which introduces a significant insertion loss–up to 4 dB [16]–due to the poor conductivity of the ACF material. This loss has been shown to critically degrade the antenna gain in such systems. In contrast, the proposed HDA avoids the use of an ACF by vertically separating the SWL-slot and SWL-dipole components. These parts are mechanically coupled using a 50 μm-thick non-conductive optically clear adhesive (OCA), thereby eliminating conductive losses and significantly improving radiation efficiency.

Lastly, the proposed SWLA adopts a 1λ array spacing, which is uncommon for phased-array-type antennas. While conventional phased arrays typically use half-wavelength spacing to prevent grating lobes and ensure a wide scanning range, the proposed 1λ spacing is employed for two reasons:

(1) to maximize the taper efficiency of the holographic metasurface; and (2) simulations confirm that a moderate scanning range is achievable without grating lobe formation, provided that the holographic metasurface fed by the SWLA consists of unit cells much smaller than half a wavelength. A detailed discussion of this design strategy and its validation are presented in Section VI-A.

C. SWLA OPERATING MECHANISM
Fig. 3 shows the variation in the reflection coefficients of the single SWL element as a function of the design parameters w_{slot}, l_{slot}, and l_{dipole}. It can be observed that w_{slot} determines the resonant frequency of the proposed SWL, whereas l_{slot} and l_{dipole} simultaneously adjust the degree of impedance matching at the resonant frequency. The parameters were optimized to set 28 GHz as the center frequency of the -10 dB impedance bandwidth. Notably, in the remainder of this work, the optically transparent mesh-grid RF ground used for SWLA and HDA is replaced with a solid PEC ground in the simulations, to reduce unnecessary
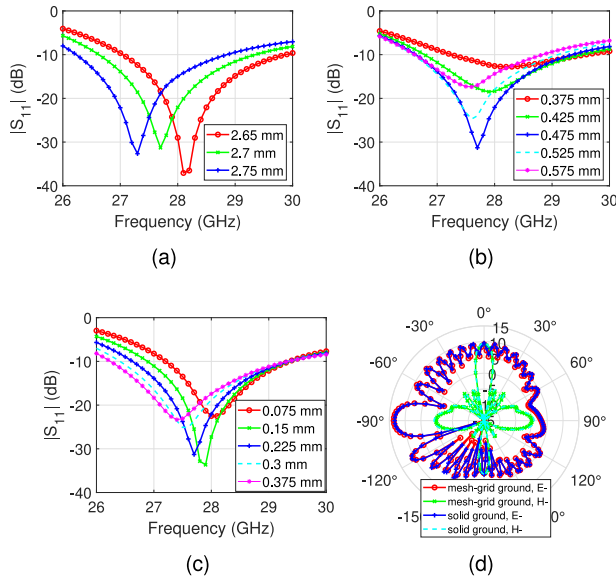
FIGURE 3. Variation in the reflection coefficient of a single SWL element as a function of (a) w_{slot}, (b) l_{slot}, and (c) l_{dipole}. (d) Comparison of the simulated radiation patterns of the SWLA using two different ground implementations: a solid PEC ground and an optically transparent mesh-grid RF ground.
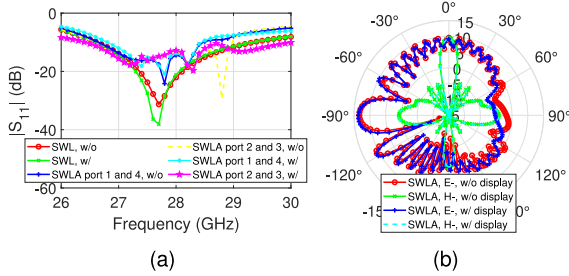

FIGURE 4. (a) Simulated reflection coefficients of a single SWL and a 1×4 SWLA (with port numbers corresponding to those defined in Fig. 2(a)); (b) radiation patterns of the 1×4 SWLA with 10.7 mm element spacing and uniform input phase, shown with and without display layers beneath the cover glass.

computational time and resource consumption. To validate this substitution, Fig. 3(d) compares the simulated radiation patterns of the SWLA with two ground implementations: a solid PEC ground and a realistic optically transparent mesh-grid RF ground. The results show that the radiation patterns are nearly identical in both cases–including the surface-wave-induced endfire lobes and local fluctuations–demonstrating that the surface-wave excitation characteristics of the SWLA are largely insensitive to the choice of the ground type.

Fig. 4(a) shows the simulated reflection and active reflection coefficients of the SWL element and a 1×4 SWLA with an array spacing of 10.7 mm (1λ), with and without display layers other than the cover glass. The reason of choosing a 1λ array spacing will be explained later. For ease of simulation, the ground at the bottom of the cover glass was assumed to be solid. It was confirmed that the existence of display layers in the plane with the SWL dipoles and GCPW does not affect the impedance matching of the SWLA.
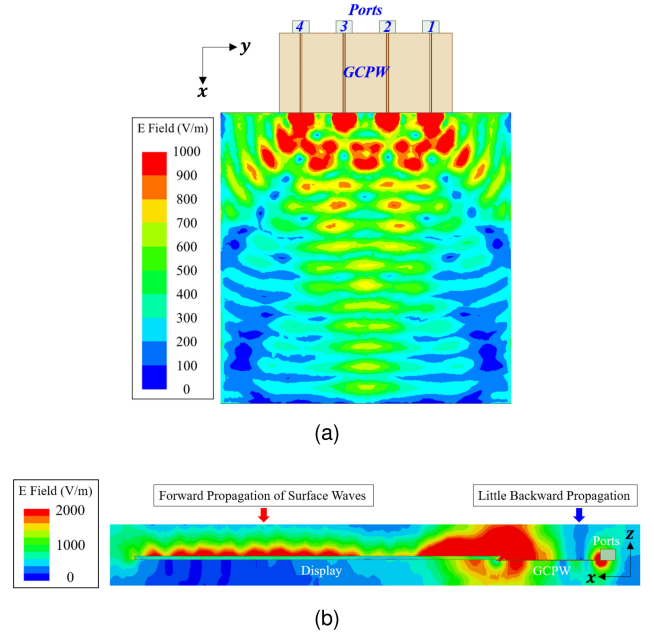

FIGURE 5. Electric field magnitude plots: (a) top view (XY-plane cut) of the electric field magnitude on the cover glass; (b) cross-sectional view (XZ-plane cut) of the complex electric field magnitude across the display cover glass and GCPW.

Fig. 4(b) shows the simulated E-plane (XZ-plane) and H-plane (YZ-plane) x-polarized radiation patterns of the SWLA without the holographic metasurface. The patterns are shown for two configurations, with and without the display stack located beneath the cover glass. In both cases, the cover glass was included, whereas the remaining display layers (polarizer, OCA, and OLED panel) were selectively added or removed. The entire display area is treated as an effective aperture that contributes to surface-wave radiation to reflect realistic application scenarios. A comparison of the two configurations demonstrates that the radiation patterns remained nearly identical, indicating that the display layers have a negligible impact on the impedance matching and radiation characteristics of the SWLA. This confirms that the SWLA can effectively excite a surface wave on the cover glass regardless of the presence of the remaining display stack components.

The endfire radiation patterns shown in Fig. 4(b) and the magnitude plot of the electric field in Fig. 5(a) further demonstrate that the proposed SWLA successfully excites the surface waves that propagate along the grounded cover glass, with the main beam directed tangentially toward its surface. Additionally, the complex electric field magnitude shown in Fig. 5(b) confirms that the proposed SWLA generates surface waves that predominantly propagate in the forward x-direction with minimal backward-propagating components. This validates the directional excitation capability of the SWL configuration, even in the absence of a dedicated reflector.

Notably, the proposed SWL shares the fundamental surface-wave-exciting principle with slot-type

SWLs [43], [50], [52]. However, it is an optimal choice for the desired HDA design because of its unique component-separated structure, which eliminates the bonding loss caused by ACF bonding in previous display antennas. In addition, not requiring an antenna substrate offers a significant advantage in the industry, where low-profile mmWave devices are highly desirable. Finally, its thickness is less than 1 mm along the x-axis, making it suitable for embedding within a thin display bezel area.

III. HOLOGRAPHIC METASURFACE ANTENNA PRINCIPLE

In this section, the principle of the holographic metasurface antenna is briefly revisited for better understanding. After empirical findings showed that using a modulated surface wave or a sinusoidally modulated surface wave structure enables the design of high-gain endfire antennas, the radiation mechanism was theoretically analyzed in [55]. It was found that the same design formulas were coherent with the holography principle used in optics that can be applied to antenna design [40]. Assuming the surface wave as the reference wave, ψ_{ref}, and the radiated wave we desire to obtain as the object wave, ψ_{obj}, the required TM_0 surface impedance at an arbitrary location on the grounded dielectric slab (GDS) fed by a SWL is calculated as follows [40]:

$$Z_s = j \times X_s = j \times \left[X + M \times Re\left(\psi_{ref}^* \psi_{obj} \right) \right], \quad (1)$$

where X is the average surface reactance value and M is the difference between the maximum and average reactance values of the predetermined unit cell type. Assuming a uniform surface wave amplitude, the required surface reactance can be rewritten as follows [40]:

$$X_s = X + M \times \cos\left(-\phi_{ref} + \phi_{obj} \right). \quad (2)$$

Numerous holographic metasurface unit cell types can be arranged on the GDS. It is revealed in [45] that there are tendencies for gain and aperture efficiency to increase as X decreases, the side-lobe level to improve but gain to decrease as M/X increases, and gain to increase but aperture efficiency to decrease as the GDS area increases. Once the unit cell type is determined, the TM_0 mode surface impedance Z_s can be calculated as follows [40]:

$$Z_s = Z_0 \sqrt{1 - n_0^2} = Z_0 \sqrt{1 - \left(\frac{\phi c}{a \omega_t} \right)^2}, \quad (3)$$

where Z_0, n_0, ϕ, c, a, and ω_t are defined as the free-space wave impedance, refractive index, phase difference, light speed, unit cell size, and surface wave frequency. A unit cell with particular design parameters is then arranged at the location where its surface impedance, calculated using (3), matches the required surface impedance, calculated using (2).
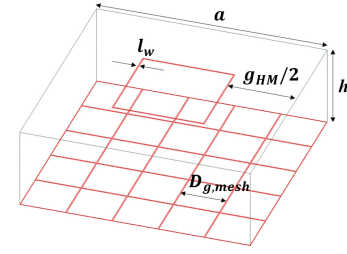

FIGURE 6. Illustration of the proposed optically transparent single-ring-type holographic metasurface unit cell (HMUC), with dimensions. The metal layer is composed of 600 nm aluminum.

IV. OPTICALLY TRANSPARENT HOLOGRAPHIC METASURFACE: UNIT CELL DESIGN

Fig. 6 shows the selected single-ring-type holographic metasurface unit cell (HMUC), consisting of a fine-metal ring and a metal-mesh ground with a 10 μm linewidth and 600 nm thick aluminum, printed on the top and bottom of the cover glass. This specific ring-type HMUC, unlike previously studied patch-type HMUCs [38], [39], [40], [41], [42], [43], [44], was selected to achieve the highest possible optical transparency (OT) by minimizing the conductor area. First, the holographic metasurface unit cell used for the HDA design should satisfy two crucial requirements. First, they should be optically transparent by having a maximum linewidth lesser than 11 μm and a pattern and unit cell OTs greater than 70% [33]. Second, the system should maintain an appropriate surface reactance range, represented by X and M in (2), at the target frequency. In this study, the target frequency is 28 GHz, which is commonly used for 5G mmWave communication. Notably, although the actual glass used in commercial smartphones is a tempered cover glass with a relative permittivity of $\epsilon_r = 6.9$ and a loss tangent of $\tan \delta = 0.004$ [25], the simulation model employs Eagle XG glass, which exhibits $\epsilon_r = 5.27$ and $\tan \delta = 0.003$. Eagle XG glass was chosen because of its dielectric similarity to actual display glass and compatibility with photolithographic fabrication processes. Although Eagle XG glass was used for the simulation, the holographic metasurface unit cell design can be appropriately scaled and optimized to achieve dispersion characteristics comparable to those of the actual material by compensating for the difference in permittivity.

Fig. 7(a) shows the simulated dispersion curves with variations in the unit cell size a and the other design parameter, g_{HM}. The Eigenmode solver provided in HFSS was used for the simulation. Notably, a solid sheet-ground assuming an ideal metal thickness and a 0.1 mm linewidth was applied for the unit cell simulation at this stage for ease of simulation. Fig. 7(b) shows the calculated surface reactance of the holographic metasurface unit cell with different values of a, using (3), where ϕ is exported from the HFSS simulation to be 36.67°, 72.95°, and 140.25° for $a = 1, 2,$ and 3 mm, respectively. In (2), X is extracted to be 239.9Ω, 330.5Ω, and 612.8Ω for $a = 1, 2,$ and 3 mm, respectively. M is extracted to be 57.2Ω, 132.2Ω, and 217.9Ω
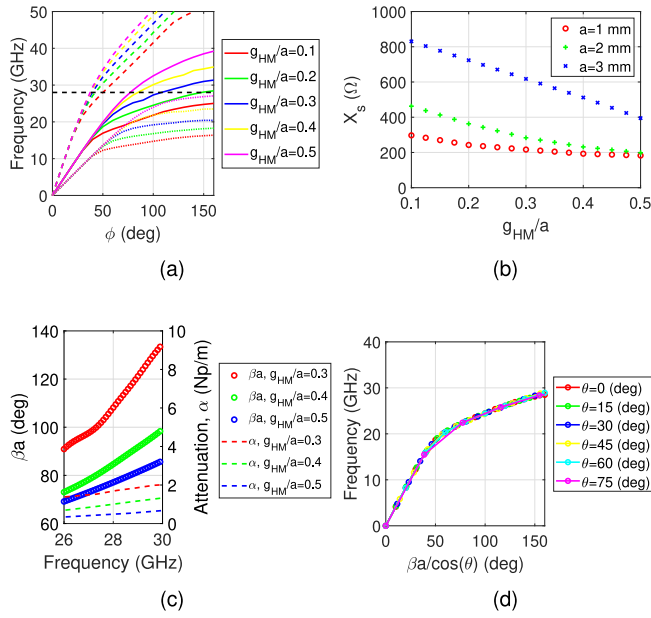
FIGURE 7. (a) Simulated dispersion curves, where dashed (- -), solid (-), and dotted (:) lines represent *a* values of 1, 2, and 3 mm, and the black dashed line indicates 28 GHz. (b) Calculated surface reactance curves showing the variations in *a* and g_{HM}. (c) Dispersion diagram including the attenuation constant α. (d) Angle dependence of a dispersion diagram for the HMUC with $g_{HM}/a = 0.2$ and $l_w = 0.1$ mm.

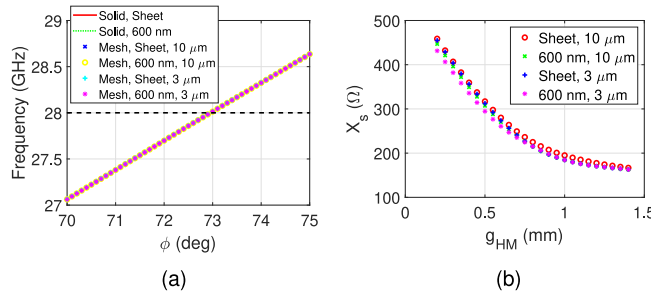**FIGURE 8.** (a) Simulated dispersion curves for the solid- or mesh-grounded unit cell without a ring pattern, showing the phase difference per cell, ϕ. The term 'sheet-ground' refers to an ideal infinite metal thickness model provided by the HFSS simulation. (b) Calculated surface reactance of the HMUC with variations in the design parameters g_{HM}, l_w, and *t*.

for $a = 1$, 2, and 3 mm, respectively. $a = 1$ mm may be the choice for the highest gain because the HMA gain increases as X decreases, as explained in Section III. However, in the HDA design, the OT decreases as *a* decreases since metal density increases. Therefore, a unit cell size of 2 mm is chosen to obtain both a high gain and high OT. Fig. 7(c) shows the dispersion diagram, including the attenuation constant α within the frequency range of interest. Fig. 7(d) shows the angle dependence of the dispersion diagram for the HMUC with $g_{HM}/a = 0.2$. It is evident that the proposed HMUC does not depend on the direction of the surface wave propagation.

Fig. 8(a) shows the simulated dispersion curves for a solid- or mesh-grounded unit cell without a ring pattern printed on the cover glass. From these dispersion curves, the phase difference, ϕ, per unit cell is determined. It can be seen

that whether or not the ground is solid, and regardless of the thickness and linewidth of the mesh-ground, ϕ has a similar value. For instance, ϕ is 72.95° for the unit cell with aluminum layers with a linewidth of 3 μm and a thickness of 600 nm. Therefore, it is confirmed that the phase difference in the surface wave propagation across a unit cell is not affected by the choice of type of ground, or by the thin linewidth and thickness of the ring pattern and mesh ground.

Finally, Fig. 8(b) shows the calculated TM_0 mode surface reactance of the HDA unit cells with variations in g_{HM}, l_w, and metal thickness *t*. It can be seen that a similar and sufficient reactance range is maintained despite the super-thin linewidth and thickness of the aluminum layers, with X and M in the range of 297.2Ω to 312.7Ω and 134.2Ω to 146.0Ω, respectively. For the case of $l_w = 10$ μm and $t = 600$ nm, X and M are 304.9Ω and 141.9Ω, respectively. Therefore, the proposed single-ring-type unit cell is an appropriate choice as an optically transparent holographic metasurface unit cell because it has a high OT and an appropriate surface reactance range that is insensitive to the linewidth and thickness of the metal patterns.

V. HOLOGRAPHIC DISPLAY ANTENNA (HDA) DESIGN PROCEDURE AND IMPORTANT DESIGN PARAMETERS
A. HDA DESIGN PROCEDURE
Once the unit cell type and its surface reactance, parameterized by design variable *g*, are determined, the holographic metasurface can be implemented over the cover glass. Based on equations (1)–(3), this metasurface can be synthesized to radiate in the desired direction when excited by an arbitrary surface wave distribution. Notably, the holographic metasurface antenna exhibits high-gain characteristics with a wide GDS area despite a relatively low aperture efficiency [45]. In this study, a 1×4 SWLA was used as the surface-wave source to steer the high-gain beam of the holographic metasurface. To present the conclusion before detailing the design procedure, the linewidth l_w of the holographic metasurface, the array spacing *d*, and the phase offset ϕ_{offset}, representing a uniform object wave phase distribution such that $\phi_{obj} = \phi_{offset}$, were optimized to be 10 μm, 1λ, and π, respectively, for the highest gain and sufficient scan ranges along with high OT. Fig. 9 summarizes the entire design procedure of the HDA, including the HFSS-exported reference wave phase distribution, the g_{HM} distribution calculated using (1)-(3), and an illustration of the final HDA design. The HM ground was composed of a metal-mesh, as shown in Fig. 6, and was fabricated and measured accordingly.

Fig. 10(a) shows the simulated reflection coefficient of the HDA compared to that of the SWLA. The operational bands for the inner and outer ports of the HDA and SWLA are nearly identical, indicating that the HM ring patterns do not affect the impedance matching of the SWLA. Notably, the HDA achieves a -10 dB impedance bandwidth of 2.30 GHz (26.67-28.97 GHz) for the inner ports and 1.68 GHz (26.72-28.40 GHz) for the outer ports. Although this is narrower
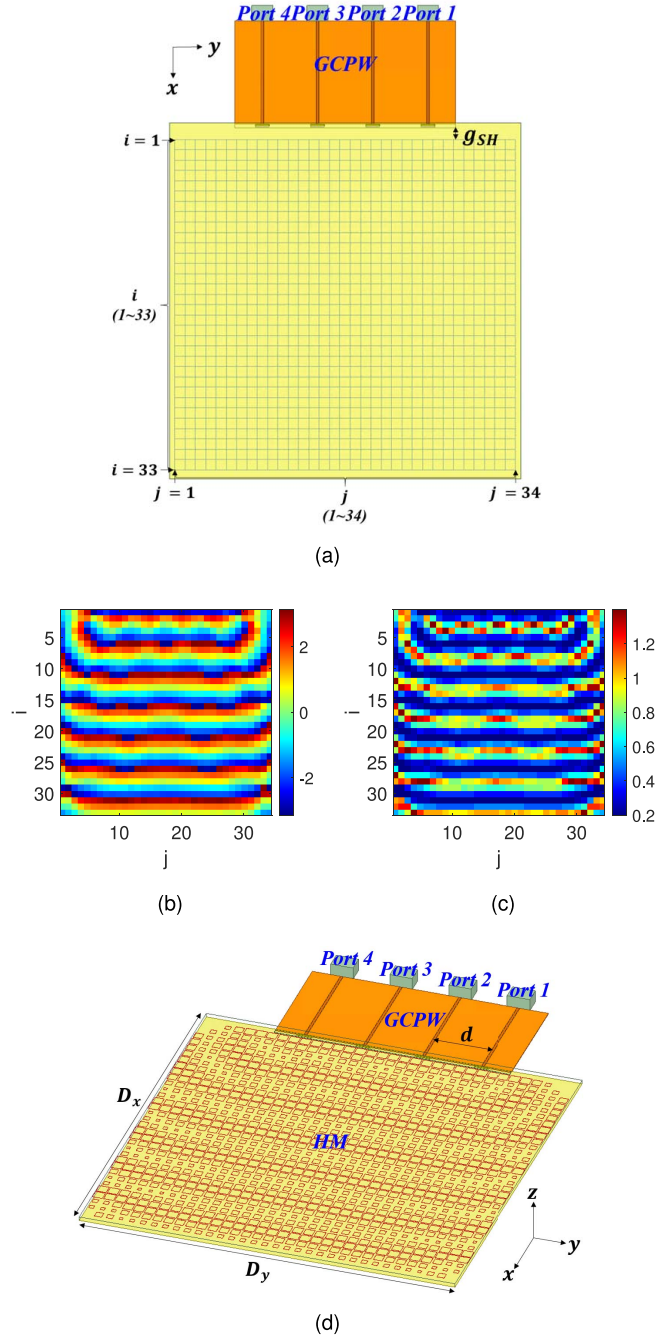
(a)

(b)

(c)

(d)

FIGURE 9. (a) The HDA without holographic ring patterns on the glass, showing points where ϕ_{ref} is captured. The design is sized to fit within a 4-inch wafer for fabrication. (b) HFSS-exported ϕ_{ref} and (c) calculated g_{HM} distributions, and (d) an illustration of the fabricated HDA.
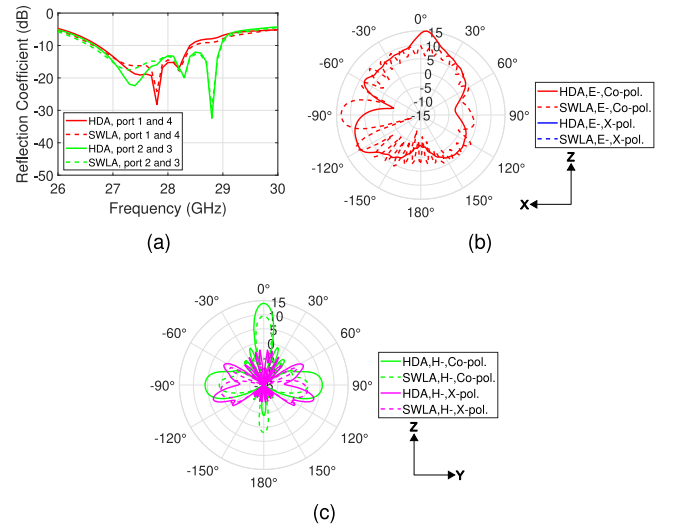

FIGURE 10. Simulated results of the SWLA with and without the holographic metasurface: (a) reflection coefficients (port numbers correspond to those defined in Fig. 9); (b) E-plane and (c) H-plane radiation patterns, all evaluated at the resonant frequency. The SWLA combined with the holographic metasurface corresponds to the proposed HDA.

than that reported in the authors' previous study [25], it is broader than the typical antenna-on-display (AoD) examples (1.8 GHz in [16] and 1.01 GHz in [17]).

While the HDA does not cover the entire mmWave band around 28 GHz, including bands n257 and n258, it does encompass the n261 band, currently employed by operators in the largest 5G mmWave service areas in the U.S. Notably, the HDA also provides a wide −3 dB gain

bandwidth of 3.28 GHz, from 26.35 GHz to 29.63 GHz, which includes the n257 band with the gain exceeding 12 dBi, as shown in Fig. 11(b). This broad gain bandwidth is due to a wide −6 dB impedance bandwidth of 3.02 GHz (26.17-29.19 GHz) for the inner ports and 3.00 GHz (26.24-29.24 GHz) for the outer ports. Therefore, while the n261 band serves as the primary operational bandwidth of the proposed HDA, the n257 band may also be a candidate operational bandwidth, depending on the user application.

Fig. 10(b) shows the simulated radiation patterns of the HDA in comparison with those of the SWLA. It is evident that the endfire lobe and large ripples present in the SWLA radiation patterns are entirely removed from those of the HDA. In addition, the main beam is directed in the broadside direction at $(\theta, \phi) = (4°, 180°)$, with a −3 dB beamwidth of 17° in the xz-plane (E-plane) and 15° in the yz-plane (H-plane). Notably, removing ripples caused by surface waves excited by conventional display antennas positioned at the edge of the display is crucial for stable communication because gain significantly decreases at the troughs of these ripples. For instance, at the main beam direction $(\theta, \phi) = (4°, 180°)$, a gain difference of 9.0 dB is observed between the HDA and the SWLA.

B. EFFECT OF LINEWIDTH, L_W, AND DISCUSSION ON BANDWIDTH

Two HDAs were designed and simulated with different l_w values: 3 μm and 10 μm for the metal-mesh ground and fine-metal ring patterns of the holographic metasurface. These l_w values were chosen to be less than 11 μm, ensuring a sufficient level of OT even for individuals with good vision [33]. Fig. 11 illustrates that the HDA with l_w =10 μm exhibits similar impedance bandwidth but higher gain and
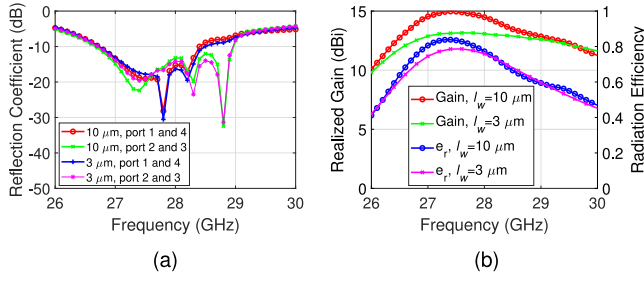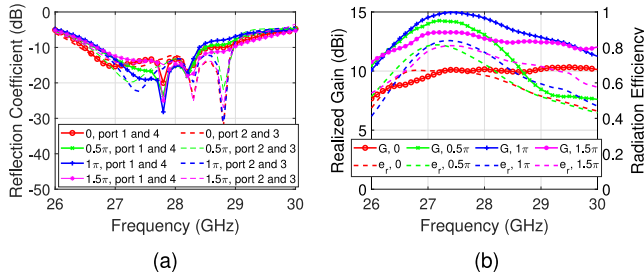
FIGURE 11. Simulated (a) reflection coefficient (port numbers correspond to those defined in Fig. 9) and (b) realized gain and radiation efficiency (e_r) of the HDAs with $l_w = 3$ μm and 10 μm.

FIGURE 12. Simulated (a) reflection coefficient (port numbers correspond to those defined in Fig. 9) and (b) realized gain (G) and radiation efficiency (e_r) of the HDAs with $\phi_{offset} = 0, 0.5\pi, 1\pi,$ and 1.5π.

radiation efficiency around center frequency than that with $l_w = 3$ μm, with a maximal gain and efficiency difference of 1.85 dB at 27.4 GHz and 6.0% at 27.2 GHz, respectively. It provides a peak gain and peak radiation efficiency of 15.0 dBi and 84% at 27.4 GHz, respectively. Notably, the HDA with $l_w = 10$ μm has a wide -3 dB-gain-bandwidth of 3.28 GHz (26.35-29.63 GHz), which covers n257 band (26.5-29.5 GHz). Although the super-thin linewidth and thickness of the HMUC pattern do not impede surface-wave propagation as severely as in the case of transmission-line-based resonant-type AoDs, the higher resistivity of the super-thinned ring patterns exacerbates their radiation efficiency. Therefore, l_w was determined to be 10 μm for higher gain and radiation efficiency while ensuring high OT. Notably, an l_w of 3 μm is also a good choice, as it exhibits sufficiently high peak gain of 13.2 dBi at 27.6 GHz with a wide -1 dB-gain-bandwidth of 2.87 GHz (26.62-29.49 GHz), which covers most of the n257 band.

C. EFFECT OF PHASE OFFSET, ϕ_{OFFSET}, IN SURFACE WAVE EXCITATION

In the design of the holographic metasurface, ϕ_{obj} in (2) was assumed to be uniform across the aperture to ensure that the boresight beam points in the normal direction, while ϕ_{ref} is derived from HFSS simulation, assuming identical input phase at each port of the SWLA. Because the surface wave excitation provided to the holographic metasurface varies depending on the unit cells adjacent to the low-profile SWLA, different values of ϕ_{obj} that are to
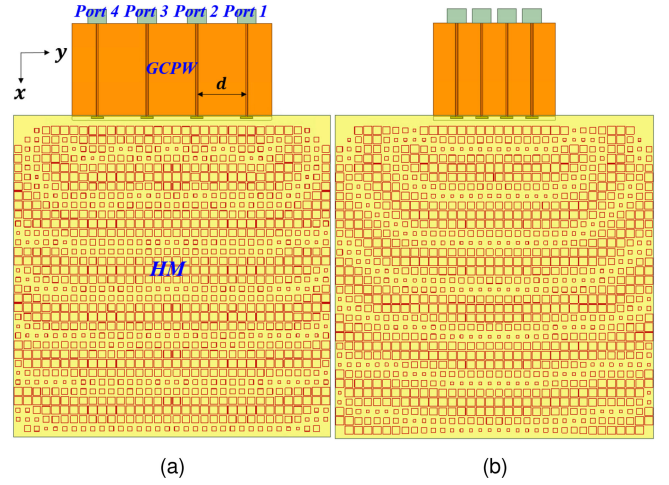

FIGURE 13. Illustration of the two simulated HDAs with different array-spacings d: (a) 1λ (10.7 mm) and (b) 0.5λ (5.35 mm).
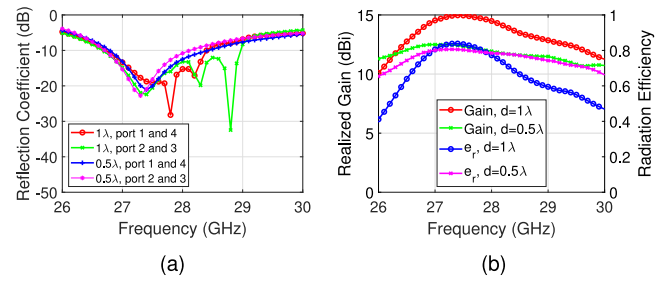

FIGURE 14. Simulated (a) reflection coefficient (port numbers correspond to those defined in Fig. 9) and (b) realized gain and radiation efficiency (e_r) of the HDAs with $d = 1\lambda$ and 0.5λ.

be uniformly assigned to the unit cells should be tested to achieve the best performance of the HDA. This specific constant value is defined in this paper as ϕ_{offset}, such that $\phi_{obj} = \phi_{offset}$. For instance, $\phi_{offset} = 0, 0.5\pi, \pi,$ and 1.5π were tested in the HDA design, as shown in Fig. 12. ϕ_{offset} was determined to be π due to its highest gain and -3 dB gain bandwidth, while maintaining sufficient radiation efficiency.

VI. DESIGN PROCEDURE OF BEAM-SCANNING HDA
A. EFFECT OF ARRAY SPACING, D, AND BEAM-SCANNING OF HDA

Fig. 13 depicts two design examples of the proposed HDA, with d equal to either one wavelength (1λ) or a half wavelength (0.5λ). Fig. 14 shows that the HDA with $d = 1\lambda$ exhibits a wider impedance bandwidth than the 0.5λ design, achieving a significantly higher gain across a broad frequency range around the 28 GHz frequency and a 2.48 dB higher peak gain, despite a lower radiation efficiency due to the reduced impedance bandwidth. Notably, a higher gain for the conventional phased-array antenna with greater array spacing stems from the effect of a wider aperture area [56]. In the case of HDA, this is also attributed to the surface wave being more evenly fed on the holographic metasurface with a greater array spacing, resulting in a
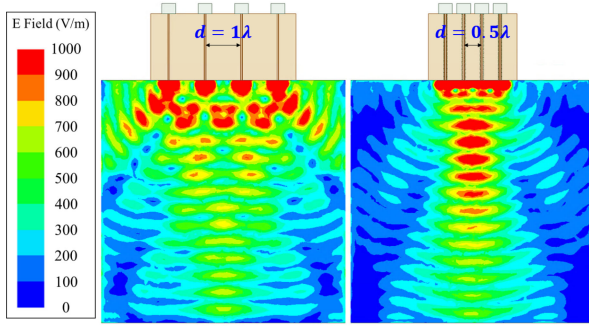
FIGURE 15. Electric field magnitude plots on the glass without holographic metasurfaces, with $d = 1\lambda$ and 0.5λ.
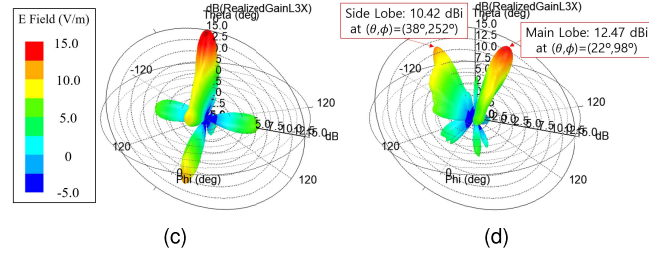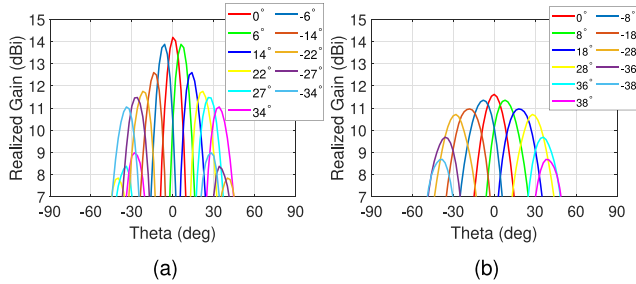

(a)

(b)

(c)

(d)

FIGURE 16. Simulated radiation patterns of the HDAs at 28 GHz: (a) scanned patterns for $d = 1\lambda$ in the azimuth plane of $\pm110°$; (b) scanned patterns for $d = 0.5\lambda$ in the azimuth plane of $\pm90°$; (c) 3D radiation pattern at broadside ($\theta = 0°$); (d) 3D radiation pattern at the maximum scan angle ($\theta = 22°$).

(a)

(b)

(c)

(d)

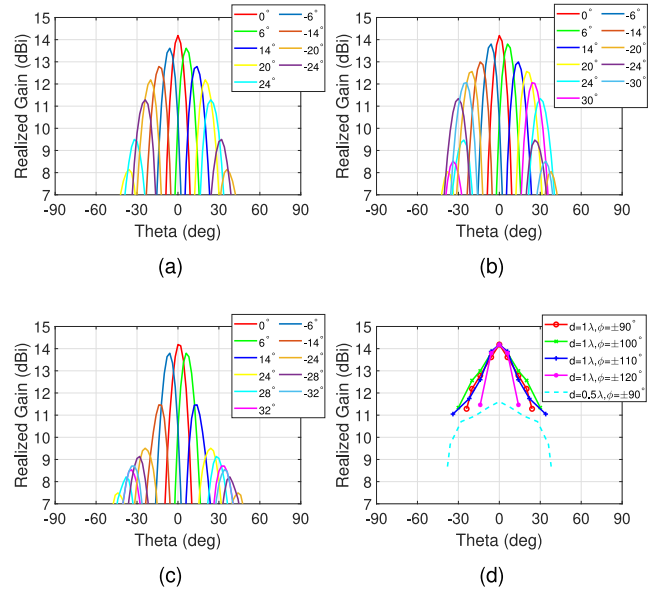**FIGURE 17.** Simulated scanned radiation patterns of the HDAs with $d = 1\lambda$ in the plane with azimuth angles of (a) $\pm90°$, (b) $\pm100°$, (c) $\pm120°$, and (d) -3 dB scanned pattern envelopes for (a)-(c) and Fig. 16(a) and (b), at 28 GHz.

higher taper efficiency [57]. The electric field magnitude plots of the front glass excited by the SWLA without holographic metasurfaces, as shown in Fig. 15, corroborate this fact.

Conventional phased-array antennas typically adopt half-wavelength element spacings to prevent grating lobes during beam steering. In contrast, the proposed HDA achieves a moderate scan range of $\pm22°$, despite the use of a 1λ-spaced SWLA, primarily because the radiation from the holographic metasurface–whose unit cell spacing is only 0.187λ–dominates the overall radiation pattern, rather than the 1λ-spaced SWLA alone. This is supported by Figs. 10(b) and 10(c), which show a difference of approximately 5 dB in the broadside gain between the HDA and SWLA-only configurations. Figs. 16(a) and 16(b) illustrate the scanned radiation patterns in the H-plane and their envelopes for HDAs with element spacing of $d = 1\lambda$ and 0.5λ, respectively. While the –3 dB gain scan range is $\pm34°$ for the former and $\pm44°$ for the latter, the 1λ-spaced HDA exhibits a higher overall envelope, with a notably higher broadside gain of 14.19 dBi which is 2.58 dB higher than the 0.5λ case. It is important to note that grating lobes must be considered when estimating realistic scan ranges. According to a representative AoD study in [16], Fig. 20(a) of that work and its accompanying explanation define the scan range of 40° when the gain difference between the main beam at $\theta = -40°$ and the sidelobe at 30° is approximately 2 dB. Based on this precedent, we similarly define the scan range as the angular span over which the main beam maintains at least a 2 dB gain advantage over the highest sidelobe. Figs. 16(c) and (d) show the 3D radiation pattern plots for both broadside and maximum scan angles. These results confirm that the realistic scan range is $\pm22°$, which is narrower than the $\pm34°$ –3 dB gain scan range.

This analysis confirms that the HDA with $d = 1\lambda$ facilitates the design of a high-gain, beam-steerable HDA. Notably, unlike a linear phased array antenna placed parallel to the y-axis, where the main beam scans at an azimuth angle of 90°, the HDA with $d = 1\lambda$ shows main beam scanning at azimuth angles of ±90-$110°$. This azimuthal rotation of the scanning plane was caused by the asymmetric arrangement of the holographic metasurface along the x-axis relative to the SWLA.

Fig. 17 presents the beam-scanned patterns of the $d = 1\lambda$ HDA in additional planes with azimuth angles of $\pm90°$, $\pm100°$, and $\pm120°$, as well as their envelopes, alongside those of the $\pm110°$ HDA and the $d = 0.5\lambda$ HDA. It shows that the $d = 1\lambda$ HDA achieves significantly higher gain and improved beam coverage within azimuth angles of ±90-$110°$.
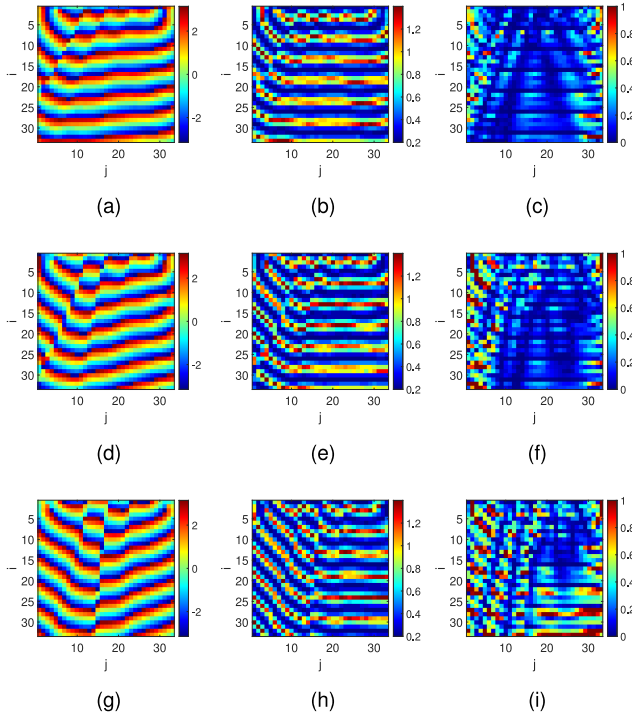
FIGURE 18. (a), (d), (g): HFSS-exported ϕ_{ref} distributions on the display region using the same method as in Fig. 9(b), with input phase progressions of 45°, 90°, and 135° assigned to port 1 through 4, respectively. (b), (e), (h): Calculated g_{HM} distributions for (a), (d), and (g). (c), (f), (i): Normalized error ($= |(X_s - X_{s0})/X_{s0}|$), where X_{s0} is the surface reactance of the proposed HDA shown in Fig. 9, and X_s corresponds to (b), (e), and (h).

B. G_{HM} DISTRIBUTION FOR BEAM-SCANNING HDA

In the previous subsection, the g_{HM} distribution on the HM, which determines the ring size of the HMUCs, was calculated simply using equation (2). This was achieved by setting ϕ_{ref} as obtained from the HFSS simulation with equal input phase assigned to Ports 1 through 4, and by defining $\phi_{obj} = \phi_{offset}$, where ϕ_{offset} is an optimized constant, assuming that the object wave or target beam pattern is a broadside beam. A natural question arises: is it correct to apply the same HM configuration for the beam-scanned HDA, given that the reference wave (ϕ_{ref}) and the object wave (ϕ_{object}) will both vary with the phase progression assigned to the four ports of the HDA? The answer is yes.

Fig. 18 presents the HFSS-exported ϕ_{ref}, g_{HM}, and normalized reactance error for different input phase progression values of 45°, 90°, and 135°. The surface reactance equation (2) has been now revised as follows:

$$X_s = X + M \times \cos\left(-\phi_{ref} - \phi_{progress} \times aj/d + \phi_{offset}\right). \quad (4)$$

where $\phi_{progress}$ is defined as the input phase progression assigned to Ports 1 through 4. In equation (5), ϕ_{obj} now includes a phase slope in the y-axis direction to enable beam-scanning.

Notably, the phase slopes in the y-axis direction for both ϕ_{ref} and ϕ_{obj} are canceled out in equation (5) over a large portion of the HM area, as shown in Fig. 18(b), (e), and (h). The calculated surface reactance X_s for $\phi_{progress} = 45°, 90°,$

and 135° are compared with X_{s0}, which is calculated for the proposed HDA, as shown in Fig. 10, by evaluating the normalized reactance error, which is defined as follows:

$$Error = |(X_s - X_{s0})/X_{s0}|. \quad (5)$$

The calculated normalized errors are shown in Fig. 18(c), (f), and (i), demonstrating that the proposed HDA can realize the required surface reactance profiles–derived from equations (1)–(3) for various input phase progression values– with high accuracy. This confirmed that the metasurface enabled beam scanning with a low synthesis error in the reactance distribution. Naturally, the error increases as $\phi_{progress}$ increases, as seen in Fig. 18(i). This also explains the narrower -3 dB beam scan range in the plane with azimuth angles of ±90° compared to the plane with azimuth angles of ±100° and ±110°, as shown in Fig. 17(d).

VII. EFFECT OF HM SIZE, N_X, AND DISCUSSION ON EFFICIENCY

Display antennas have shown relatively low aperture efficiencies [16], [17], [18], [21], [22], [23], ranging from 30% to 50%, which is significantly lower than those of typical resonant-type antennas, such as patch and dipole antennas, which generally achieve high aperture efficiencies between 80% and 100%. This reduced efficiency is attributed to the high resistivity of optically transparent conductors. Given that resonant-type antennas achieve higher aperture efficiency at their resonant frequencies compared to traveling wave antennas such as the HDA, it is expected that the HDA will exhibit an aperture efficiency of less than 30-50%.

Fig. 19 shows how the aperture efficiency and realized gain vary with N_x, the number of HMUCs along the x-axis. Notably, $N_x = 0$ corresponds to the SWLA without HM, whereas $N_x = 33$ represents the proposed HDA. It is evident that the aperture efficiency decreases, whereas the realized gain increases as the HM size expands. This is due to surface wave attenuation on the HM as it gradually transforms into a radiated wave, resulting in a weaker excitation of the reference wave on the HMUCs farther from the SWLA. The electric field distribution in Fig. 19(c) indicates that the HDA gain saturates when N_x exceeds 20, as confirmed in Fig. 19(b). From the perspective of a mobile-device designer, Fig. 19(b) shows the selection of the desired gain and aperture efficiency. For example, if a gain of 13 dBi is sufficient, only ten unit cells ($N_x = 10$) can be arranged along the x-axis to achieve a high gain of 13.5 dBi with a moderate aperture efficiency of 15.0%. For example, in this study, the HM size was maximized to achieve the highest possible gain from the HDA. This is a practical decision from the standpoint of a mobile-device designer because the wide display area of mobile devices may otherwise remain unused. However, this strategy may require adjustments if multiple display antennas are actively used in the future.
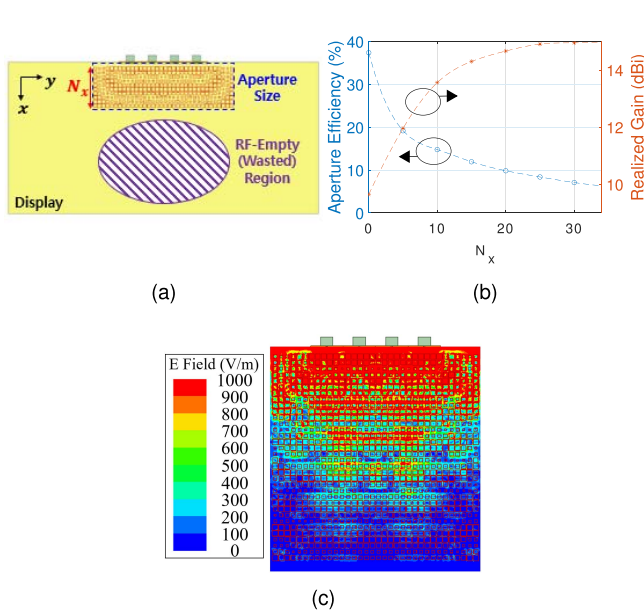
(a)

(b)

(c)

FIGURE 19. (a) Illustration of the HM aperture size and RF-empty display region in relation to the number of HMUCs along the x-axis. (b) Simulated aperture efficiency and realized gain of the HDAs with varying HM sizes, N_x, where $N_x = 0$ represents the SWLA without HM and $N_x = 33$ represents the measured HDA. (c) Magnitude of the electric field distributed on the HM.

VIII. FABRICATION AND EXPERIMENTAL RESULTS
A. FABRICATION AND MEASUREMENT

In the fabrication procedure, the HDA is divided into two parts according to the substrate: (1) the display cover glass, where an optically transparent holographic metasurface and SWLA slots are printed and (2) the dielectric substrate, where SWLA dipoles and GCPW are printed. The former is fabricated using photolithography on a 4-inch glass wafer, whereas the latter is fabricated using a general PCB fabrication process. The two parts are then manually attached using an OCA film and a microscope. Among the various fabrication technologies for transparent antennas, such as physical vapor deposition, RF sputtering, spray pyrolysis, inkjet printing, and electrospinning, photolithography was selected because of its renowned accuracy, high resolution, and feasibility for mass production [58]. Photolithography for the HDA was performed at the Inter-University Semiconductor Research Center of Seoul National University.

Fig. 20 shows the photographs of the fabricated sample, an enlarged sample viewed under a microscope, and the measurement setup in the anechoic RF chamber. It can be seen that the proposed holographic metasurface is indeed optically transparent using the selected design parameters. The holographic metasurface measures 69 mm×68 mm, and several metal patterns at the corners are removed owing to the size limitations of the fabrication machine. When the glass and PCB are attached using the OCA film, the display stack under the glass is neglected. As confirmed in Section II, the display stack does not affect the radiation characteristics of the HDA.
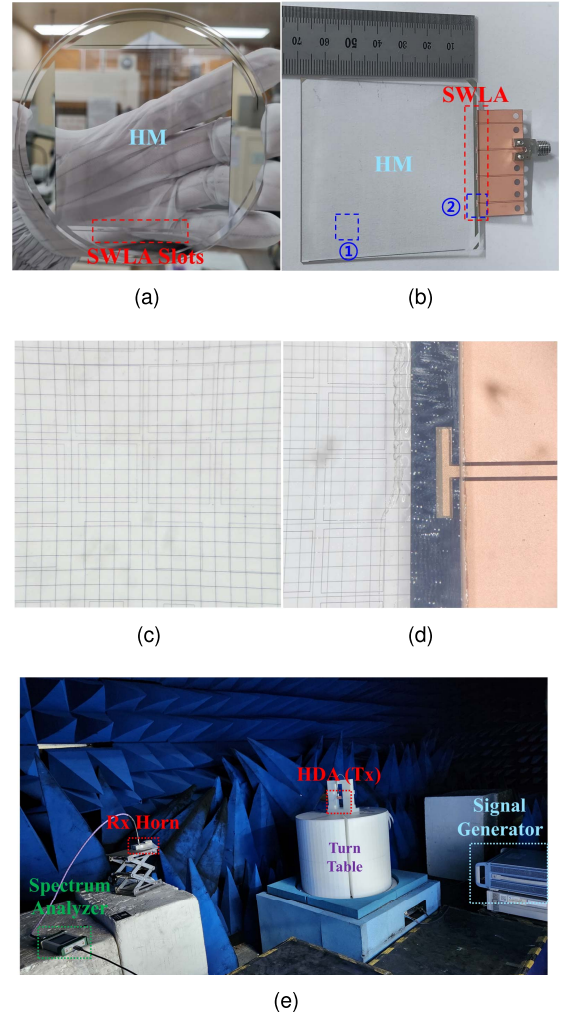

(a)

(b)

(c)

(d)

(e)

FIGURE 20. Photographs of (a) the fabricated optically transparent holographic metasurface (HM) created using photolithography on a 4-inch glass wafer, (b) the HDA sample comprising the HM, SWLA, and GCPW, (c) and (d) enlarged views of regions ⓐ and (d) ⓑ as indicated in (b)) under a microscope, and (e) the measurement setup in an anechoic RF chamber.

Fig. 21(a) shows that the simulated and measured reflection coefficients of the HDA are in good agreement. The HDA exhibits measured bandwidths of 2.39 GHz (26.78-29.17 GHz) for the inner ports and 2.03 GHz (27.10-29.13 GHz) for the outer ports, which are wider than the simulated bandwidths of 2.30 GHz (26.67-28.97 GHz) for the inner ports and 1.68 GHz (26.72-28.40 GHz) for the outer ports. The errors in the measurement results were mainly due to the manual attachment of the glass and PCB using the OCA film and a microscope. Fig. 21(b) shows that the simulated and measured gain and radiation efficiency over the frequency range are in good agreement. Notably, the simulated and measured peak gains are 14.96 dBi and 14.17 dBi at 27.5 GHz and 27.6 GHz, respectively. The simulated and measured radiation efficiencies are 0.84 at 27.4 GHz and 0.71 at 27.7 GHz. Fig. 21(c) shows that the mutual coupling coefficients remain below –10 dB across most of the n261 band (27.5–28.35 GHz). Fig. 21(d) shows
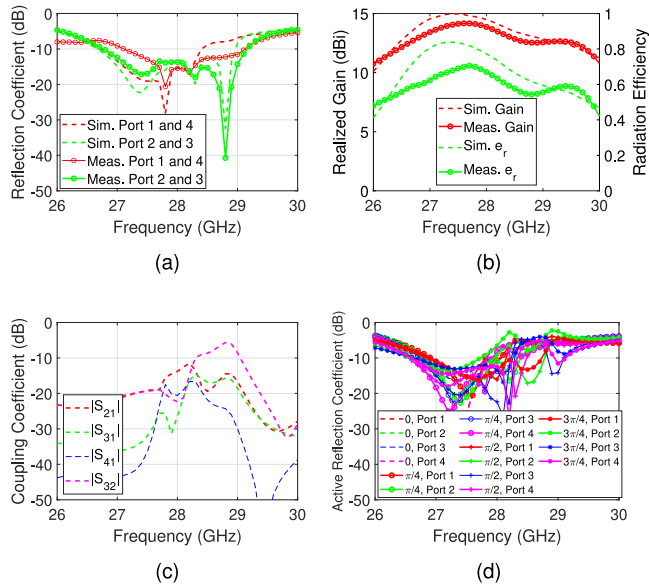
FIGURE 21. Simulated and measured results of the fabricated HDA: (a) reflection coefficients, (b) realized gain and radiation efficiency, (c) coupling coefficients, and (d) active reflection coefficients under progressive phase states with phase steps of 0, $\pi/4$, $\pi/2$, and $3\pi/4$.
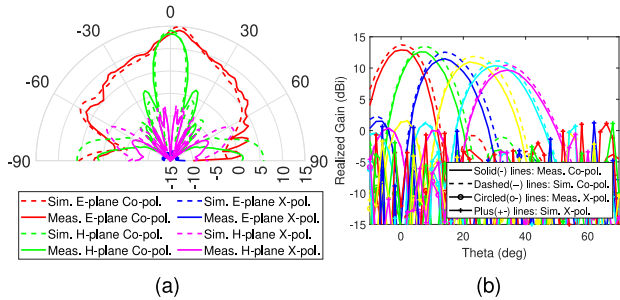

FIGURE 22. Simulated and measured (a) boresight radiation patterns in the E- and H-planes at 27.5 GHz, and (b) scanned radiation patterns in the plane with an azimuth angle of 110° for the fabricated HDA at 28 GHz.

the simulated active reflection coefficients under progressive phase excitations with phase steps of 0, $\pi/4$, $\pi/2$, and $3\pi/4$. These remain below –10 dB over a 0.82 GHz bandwidth (26.91–27.73 GHz), which is comparable to the n261 band but slightly shifted by approximately 0.6 GHz due to the array configuration. This minor frequency offset can be readily compensated through small design adjustments. In addition, the –3 dB gain bandwidth of the HDA spans 26.4–29.6 GHz, sufficiently covering the entire n261 band. These results confirm the suitability of the proposed HDA for phased-array applications.

The simulated and measured E- and H-plane radiation patterns with uniform input phases are shown in Fig. 22(a). Compared to Fig. 4(b), the large endfire lobe is completely eliminated, and the main beam with peak gain is directed in the broadside direction. Simulated and measured boresight gains at $(\theta, \phi) = (4°, 0°)$ increase by 8.96 dB and 8.17 dB, respectively, from 6.00 dBi to 14.96 dBi and 14.17 dBi, through the integration of the holographic metasurface.
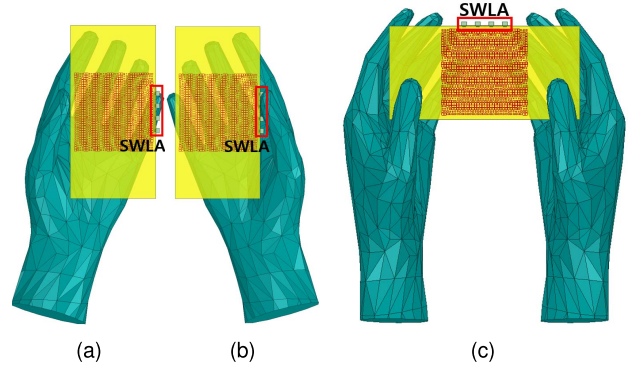

FIGURE 23. Evaluation of the antenna's radiation performance in the presence of hand phantoms under three typical usage scenarios: (a) left-hand scenario (LHS), (b) right-hand scenario (RHS), and (c) double-hand scenario (DHS). The LHS and RHS represent data usage conditions, while the DHS corresponds to the reading scenario, as described in [59].

Moreover, the undesired fluctuations in the E-plane pattern of the SWLA without the holographic metasurface is completely smoothened. In summary, the proposed HDA effectively controls the surface waves on the display cover glass. Notably, the proposed antenna achieved a high cross-polarization level in the main beam direction of $(\theta, \phi) = (4°, 0°)$, exceeding 25 dB.

The scanned radiation patterns are measured using the active element pattern technique described in [25]. The simulated and measured scanned patterns show good agreement, as illustrated in Fig. 22(b). Only the scanned radiation patterns with positive scan angles are displayed, owing to the symmetry of the antenna structure. While the measured broadside gain of 14.17 dBi is 0.79 dB lower than the simulated broadside gain of 14.96 dBi, the simulated and measured -3 dB scan ranges are comparable.

B. HAND PHANTOM EFFECTS

Although integrated within the display, the proposed HDA operates as a mobile antenna and, therefore, must be evaluated in proximity to the human body [59], a consideration that has been largely overlooked in previous studies on display antennas. Following the typical usage scenarios defined in [59], three cases were evaluated: the left-hand scenario (LHS), right-hand scenario (RHS), and double-hand scenario (DHS). The LHS and RHS correspond to the data usage conditions, whereas the DHS represents the reading scenario, which is consistent with the simulation setup shown in Fig. 23. The hand phantoms used in the simulation were sourced from the component library provided by ANSYS HFSS.

Fig. 24 shows the simulated reflection coefficients and radiation efficiencies across the frequencies in the n261 band. This demonstrates that the bandwidths of the LHS, RHS, and DHS of the inner and outer ports of the HDA adequately cover the n261 band. The bandwidths of the outer ports are widened, whereas at least 85% of the bandwidths of the inner ports were maintained. This confirms that HDA

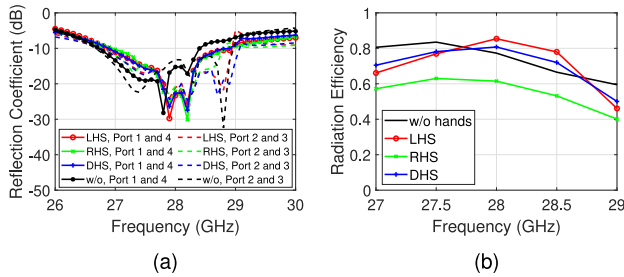**TABLE 3.** Comparison of state-of-the-art display antennas.

Ref.	[16]	[17]	[18]	[21]	[22]	[23]	[24]	[25]	**This work**
Center Frequency (GHz)	28	28	4.7/26/28	28	28/38	32	5	28	**28**
Antenna Topology	Resonant	Resonant	Resonant	Resonant	Resonant	Resonant	Traveling	Resonant	**Traveling**
Antenna Type	Patch	Patch	Patch	Slotted Dipole	Patch/ Monopole	Patch/ Monopole	CRLH	Folded Dipole	**Holographic Metasurface**
Optical Transparency	0.88	0.96	0.86	0.85	N/A	0.88	0.88	*1.0	**0.94**
Antenna Size (**$\lambda_0 \times \lambda_0$)	2.0×5.1	N/A	2.1×4.2	0.84×1.05	3.3×3.7	1.7×3.3	0.18×2.2	1.9×3.7	**6.4×6.3**
Gain (dBi)	9.16 (1×8 array)	1.7 (element)	9.6 (1×8 array)	1.12 (element)	7.17/7.2 (1×4 array)	9.45 (1×8 array)	2.68 (13 unit cells)	***9.81 (1×4 array)	**Sim.: 14.96 Meas.: 14.17 (1×4 SWLA)**
Radiation Efficiency (%)	41	N/A	61	42	N/A	****56	63	54	**Sim.: 84 Meas.: 71**
Scan Range (°)	±40	N/A	±75	N/A	±40	±35	N/A	±60	**±22**

* Located outside the display active area.

** λ_0 denotes the free-space wavelength at the center frequency. For both [18] and [22], a center frequency of 28 GHz was used to calculate λ_0.

*** Including the calibrated average feed line loss of 2.51 dB for fair comparison.

**** Assumed from the plot.

FIGURE 24. Simulated (a) reflection coefficients and (b) realized gain and radiation efficiency of the HDA under four conditions: without hand phantom, LHS, RHS, and DHS.

covers the n261 band with a sufficient margin for typical hand scenarios.

C. COMPARISON WITH PREVIOUS DISPLAY ANTENNAS
Table 3 presents a comparison between the proposed HDA and conventional display antennas. Most display antennas are designed with a resonant antenna topology, except for [24]. In general, they exhibit low gain and radiation efficiency owing to the high resistivity of optically transparent radiators and transmission lines, as well as high bonding loss. In [24], an antenna was embedded in the dead space located at the edge of an OLED panel. However, it still suffered from a low radiation efficiency. Most importantly, radiation pattern distortion, including beam tilt and undesired fluctuations in beam patterns, occurred because AoD and AiD could not control the surface waves generated on a wide display area.

By contrast, the HDA proposed in this study integrates an optically transparent holographic metasurface to transform the surface waves excited on the wide display area into high-gain radiated waves. The specially designed SWLA structure also contributed to the high gain and radiation efficiency of the HDA by eliminating bonding loss. It demonstrates an unprecedented high measured gain of 14.17 dBi, whereas other display antennas typically exhibit a gain below 10 dBi, even with a 1×8 array configuration. While the high gain of the proposed HDA benefits from its relatively large aperture, its ability to utilize the broad display area with a structurally simple configuration–based on size-varying ring patterns–is a significant advantage over conventional resonant designs that require complex feeding networks. It also exhibited the highest measured radiation efficiency of 71%, whereas the others exhibited low radiation efficiencies of less than 65%. Remarkably, the highest gain and radiation efficiency are achieved with a moderate scan range of ±22° and a high OT of 0.94 at the same time. The OT of the proposed HDA was calculated using the equation introduced in [32].

IX. CONCLUSION
This paper presents a novel traveling-wave-antenna-type HDA that utilizes surface waves over a wide display area to achieve high gain and radiation efficiency. The HDA comprises an optically transparent holographic metasurface (HM) printed on a display cover glass and a SWLA positioned on a thin display bezel area at the edge of the display. Our findings demonstrate that HDA effectively controls the surface waves, resulting in the elimination of beam distortions such as beam tilt and undesired fluctuations

in beam patterns, while achieving a high gain and radiation efficiency. Additionally, HDA achieves a beam-steering capability through the SWLA, which is essential for 5G millimeter-wave applications.

The uniquely structured SWLA is divided into two parts to mitigate the high bonding losses typically associated with conventional display antennas. The SWLA slots are printed under glass in the display bezel area and attached to the SWLA dipoles printed on a FPCB using a thin OCA film. The array spacing was set to one wavelength instead of the conventional half wavelength to improve the taper efficiency of the HM, thereby enhancing the overall gain and radiation efficiency of the antenna.

The measured bandwidths of the proposed HDA confirm that the n261 band is the primary operational bandwidth, with the n257 band as a potential candidate, depending on the user application. Future work will focus on achieving wideband operation including 28 GHz, encompassing the n257, n258, and n261 bands or dual-band operation, including the n260 band, to enhance the versatility of the proposed display antenna scheme.

REFERENCES

[1] Y. Zhang and J. Mao, "An overview of the development of antenna-in-package technology for highly integrated wireless devices," *Proc. IEEE*, vol. 107, no. 11, pp. 2265–2280, Nov. 2019.

[2] Y. P. Zhang and D. Liu, "Antenna-on-chip and antenna-in-package solutions to highly integrated millimeter-wave devices for wireless communications," *IEEE Trans. Antennas Propag.*, vol. 57, no. 10, pp. 2830–2841, Oct. 2009.

[3] Y. P. Zhang et al., "antenna-in-package design for wirebond interconnection to highly integrated 60-GHz radios," *IEEE Trans. Antennas Propag.*, vol. 57, no. 10, pp. 2842–2852, Oct. 2009.

[4] D. Liu et al., "Antenna-in-package design considerations for Ka-band 5G communication applications," *IEEE Trans. Antennas Propag.*, vol. 65, no. 12, pp. 6372–6379, Dec. 2017.

[5] J. Heo et al., "Tetra-plexing dual-broadband/dual-polarized antenna for 5G/6G millimeter-wave systems," *IEEE Trans. Antennas Propag.*, early access, May 20, 2025, doi: 10.1109/TAP.2025.3570006.

[6] S. Bang et al., "Extremely miniaturized free-space measurement system for RF metamaterial composite based on beam focusing transmitarray," *IEEE Antennas Wireless Propag. Lett.*, vol. 23, no. 6, pp. 1705–1709, Jun. 2024.

[7] H. Kim and J. Oh, "140-GHz wideband array antenna-in-package using multimode resonance," *IEEE Trans. Antennas Propag.*, vol. 71, no. 3, pp. 2136–2144, Mar. 2023.

[8] B. Kim et al., "Heterogeneous metasurface empowering proximate high-permittivity ceramic cover for a 5G dual-band millimeter-wave smartphone," *IEEE Trans. Antennas Propag.*, vol. 72, no. 5, pp. 4086–4094, May 2024.

[9] B. Kim and J. Oh, "Dual-wideband low-profile three-notch patch antenna with indirect differential feeding for 5G millimeter-wave applications," *IEEE Antennas Wireless Propag. Lett.*, vol. 24, no. 9, pp. 2734–2738, Sep. 2025. doi: 10.1109/LAWP.2025.3572958.

[10] Y. P. Zhang, M. Sun and L. H. Guo, "On-chip antennas for 60-GHz radios in silicon technology," *IEEE Trans. Electron Devices*, vol. 52, no. 7, pp. 1664–1668, Jul. 2005.

[11] H. M. Cheema and A. Shamim, "The last barrier: on-chip antennas," *IEEE Microw. Mag.*, vol. 14, no. 1, pp. 79–91, Jan. 2013.

[12] M. Alibakhshikenari et al., "A comprehensive survey on antennas on-chip based on metamaterial, metasurface, and substrate integrated waveguide principles for millimeter-waves and terahertz integrated circuits and systems," *IEEE Access*, vol. 10, pp. 3668–3692, 2022.

[13] Z. Su et al., "A dual band additively manufactured 3-D antenna on package With near-isotropic radiation pattern," *IEEE Trans. Antennas Propag.*, vol. 66, no. 7, pp. 3295–3305, Jul. 2018.

[14] Z. Su et al., "Antenna-on-package design: Achieving near-isotropic radiation pattern and wide CP coverage simultaneously," *IEEE Trans. Antennas Propag.*, vol. 69, no. 7, pp. 3740–3749, Jul. 2021.

[15] S. Oh and J. Oh, "140-GHz affordable miniaturized array antenna-on-package for sub-THz transceiver," *IEEE Access*, vol. 11, pp. 132780–132791, 2023.

[16] J. Park et al., "An optically invisible antenna-on-display concept for millimeter-wave 5G cellular devices," *IEEE Trans. Antennas Propag.*, vol. 67, no. 5, pp. 2942–2952, May 2019.

[17] J. M. Heo et al., "Characteristic impedance adjustment of thin-metal mesh transmission lines for mmWave display-integrated antennas," *IEEE Access*, vol. 9, pp. 94714–94722, 2021.

[18] H. C. Qiu et al., "Compact, flexible, and transparent antennas based on embedded metallic mesh for wearable devices in 5G wireless network," *IEEE Trans. Antennas Propag.*, vol. 69, no. 4, pp. 1864–1873, Apr. 2021.

[19] J. Park et al., "Circuit-on-display: A flexible, invisible hybrid electromagnetic sensor concept," *IEEE J. Microw.*, vol. 1, no. 2, pp. 550–559, Apr. 2021.

[20] R. Rodríguez-Cano, S. Zhang, and G. F. Pedersen, "Transparent mmwave array on a glass substrate with surface wave reduction," in *Proc. 14th Eur. Conf. Antennas Propag. (EuCAP)*, Jul. 2020, pp. 1–4.

[21] T. D. Nguyen et al., "Optically invisible artificial magnetic conductor subarrays for triband display-integrated antennas," *IEEE Trans. Microw. Theory Techn.*, vol. 70, no. 8, pp. 3975–3986, Aug. 2022.

[22] D. Lee et al., "Dual-polarized dual-band antenna-on-display using via-less and single-layer topology for mmWave wireless scenarios," *IEEE Antennas Wireless Propag. Lett.*, vol. 22, no. 5, pp. 1000–1004, May 2023.

[23] J. Park, I. Jang, B. Seong and W. Hong, "Differentially fed, 1-D phased-array antenna-on-display featuring wideband and polarization agility for millimeter-wave wireless applications," *IEEE Trans. Antennas Propag.*, vol. 71, no. 9, pp. 7196–7205, Sep. 2023.

[24] M. Kim et al., "Antenna-on-display concept on an extremely thin substrate for sub-6 GHz wireless applications," *IEEE Trans. Antennas Propag.*, vol. 70, no. 7, pp. 5929–5934, Jul. 2022.

[25] J. Oh et al., "High-gain millimeter-wave antenna-in-display using non-optical space for 5G smartphones," *IEEE Trans. Antennas Propag.*, vol. 71, no. 2, pp. 1458–1468, Feb. 2023.

[26] J. Oh et al., "Tightly embedded modular antenna-in-display (MAiD) into the panel edge of display with dual-polarization for 5G smartphones," *IEEE Trans. Antennas Propag.*, vol. 73, no. 2, pp. 1209–1214, Feb. 2025.

[27] S. Hong, S. H. Kang, Y. Kim, and C. W. Jung, "Transparent and flexible antenna for wearable glasses applications," *IEEE Trans. Antennas Propag.*, vol. 64, no. 7, pp. 2797–2804, Jul. 2016.

[28] J. -J. Peng, S. -W. Qu and M. Xia, "Optically transparent reflectarray based on indium tin oxide with improved efficiency," *IEEE Trans. Antennas Propag.*, vol. 68, no. 4, pp. 3289–3294, Apr. 2020.

[29] N. Outaleb, J. Pinel, M. Drissi, and O. Bonnaud, "Microwave planar antenna with RF-sputtered indium tin oxide films," *Microw. Opt. Technol. Lett.*, vol. 24, no. 1, pp. 3–7, 2000.

[30] C. Kocia and S. V. Hum, "Design of an optically transparent reflectarray for solar applications using indium tin oxide," *IEEE Trans. Antennas Propag.*, vol. 64, no. 7, pp. 2884–2893, Jul. 2016.

[31] S. Hong, Y. Kim, and C. Won Jung, "Transparent microstrip patch antennas with multilayer and metal-mesh films," *IEEE Antennas Wireless Propag. Lett.*, vol. 16, pp. 772–775, 2017.

[32] S. H. Kang and C. W. Jung, "Transparent patch antenna using metal mesh," *IEEE Trans. Antennas Propag.*, vol. 66, no. 4, pp. 2095–2100, Apr. 2018.

[33] B. Kim and J. Oh, "Single-glass layer optically transparent transmitarray with high aperture efficiency and low profile at 5G millimeter-wave band," *IEEE Trans. Antennas Propag.*, vol. 71, no. 11, pp. 9036–9041, Nov. 2023.

[34] B. Kim et al., "Locally optimal periods in periodic optically transparent two-metal-layered refractive metasurfaces for outdoor-to-indoor communication," *IEEE Antennas Wireless Propag. Lett.*, vol. 24, no. 5, pp. 1253–1257, May 2025.

[35] B. Kim and J. Oh, "Characterization of optically transparent two-metal-layered refractive metasurfaces for 6G upper-mid outdoor-to-indoor communication," in *Proc. IEEE Antennas Propag. Soc. Int. Symp. (APSURSI)*, Firenze, Italy, 2024, pp. 1363–1364.

[36] G. Oliveri et al., "Optically-transparent EM skins for outdoor-to-indoor mm-wave wireless communications," *IEEE Access*, vol. 12, pp. 65178–65191, 2024.

[37] R. Rodriguez-Cano et al., "mm-Wave beam-steerable endfire array embedded in a slotted metal-frame LTE antenna," *IEEE Trans. Antennas Propag.*, vol. 68, no. 5, pp. 3685–3694, May 2020.

[38] B. Kim et al., "Broadband holographic mode synthesis between adjacent resonances for a low-profile thin-microstrip antenna-fed metasurface," *IEEE Trans. Antennas Propag.*, vol. 73, no. 11, pp. 9577–9582, Nov. 2025. doi: 10.1109/TAP.2025.3590571.

[39] T. Galler et al., "High-gain millimeter-wave holographic antenna in package using glass technology," *IEEE Antennas Wireless Propag. Lett.*, vol. 19, no. 12, pp. 2067–2071, Dec. 2020.

[40] B. H. Fong et al., "Scalar and tensor holographic artificial impedance surfaces," *IEEE Trans. Antennas Propag.*, vol. 58, no. 10, pp. 3212–3221, Oct. 2010.

[41] H. -H. Lv et al., "Holographic design of beam-switchable leaky-wave antenna," *IEEE Antennas Wireless Propag. Lett.*, vol. 18, no. 12, pp. 2736–2740, Dec. 2019.

[42] Z. L. Ma et al., "A collimated surface-wave-excited high-impedance surface leaky-wave antenna," *IEEE Antennas Wireless Propag. Lett.*, vol. 16, pp. 2082–2085, 2017.

[43] S. K. Podilchak et al., "Broadside radiation from a planar 2-D leaky-wave antenna by practical surface-wave launching," *IEEE Antennas Wireless Propag. Lett.*, vol. 7, pp. 517–520, 2008.

[44] C. Rusch et al., "holographic mmW-antennas with TE0 and TM0 surface wave launchers for frequency-scanning FMCW-radars," *IEEE Trans. Antennas Propag.*, vol. 63, no. 4, pp. 1603–1613, Apr. 2015.

[45] G. Minatti et al., "Spiral leaky-wave antennas based on modulated surface impedance," *IEEE Trans. Antennas Propag.*, vol. 59, no. 12, pp. 4436–4444, Dec. 2011.

[46] Z. Chen and Z. Shen, "Wideband flush-mounted surface wave antenna of very low profile," *IEEE Trans. Antennas Propag.*, vol. 63, no. 6, pp. 2430–2438, Jun. 2015.

[47] Z. Hu, Z. Shen, and W. Wu, "Reconfigurable leaky-wave antenna based on periodic water grating," *IEEE Antennas Wireless Propag. Lett.*, vol. 13, pp. 134–137, 2014.

[48] L. Gan et al., "Low profile circularly polarized holographic antenna with improved aperture efficiency," in *Proc. Int. Conf. Microw. Millimeter Wave Technol. (ICMMT)*, 2023, pp. 1–3.

[49] Y. Liu et al., "Low RCS and high-gain patch antenna based on a holographic metasurface," *IEEE Antennas Wireless Propag. Lett.*, vol. 18, no. 3, pp. 492–496, Mar. 2019.

[50] J. -L. Liu, T. Su, and Z.-X. Liu, "High-gain grating antenna with surface wave launcher array," *IEEE Antennas Wireless Propag. Lett.*, vol. 17, no. 4, pp. 706–709, Apr. 2018.

[51] V. G. -G. Buendía et al., "2-D planar leaky-wave antenna with fixed frequency beam steering through broadside," in *Proc. 14th Eur. Conf. Antennas Propag. (EuCAP)*, 2020, pp. 1–4.

[52] S. K. Podilchak et al., "Surface-wave launchers for beam steering and application to planar leaky-wave antennas," *IEEE Trans. Antennas Propag.*, vol. 57, no. 2, pp. 355–363, Feb. 2009.

[53] J. Tang et al., "Optically transparent anisotropic holographic impedance metasurface for launching orbital angular momentum vortex wave," *J. Phys. D Appl. Phys.*, vol. 56, p. 39, Jun. 2023.

[54] D. M. Pozar, *Microwave Engineering*, 3rd ed. Hoboken, NJ, USA: Wiley, 2005.

[55] A. Oliner and A. Hessel, "Guided waves on sinusoidally-modulated reactance surfaces," *IRE Trans. Antennas Propag.*, vol. 7, no. 5, pp. 201–208, Dec. 1959.

[56] A. K. Bhattacharyya, *Phased Array Antennas: Floquet Analysis, Synthesis, BFNs and Active Array Systems*. Hoboken, NJ, USA: Wiley, 2006.

[57] A. Yu et al., "Aperture efficiency analysis of reflectarray antennas," *Microw. Opt. Technol. Lett.*, vol. 52, no. 2, pp. 364–372, 2010.

[58] A. S. M. Sayem et al., "Flexible transparent antennas: Advancements, challenges, and prospects," *IEEE Open J. Antennas Propag.*, vol. 3, pp. 1109–1133, 2022.

[59] Y. Li et al., "12-port 5G massive MIMO antenna array in sub-6GHz mobile handset for LTE bands 42/43/46 applications," *IEEE Access*, vol. 6, pp. 344–354, 2018.

BYEONGJIN KIM (Graduate Student Member, IEEE) received the B.S. degree in electrical and computer engineering from Seoul National University, South Korea, in 2020, where he is currently pursuing the integrated master's and Ph.D. degrees. His current research interests include display antenna, antenna-in-package, optically transparent antenna, transmitarray, reflectarray, metasurface antenna, and holographic metasurface antenna for 5G millimeter-wave, 6G upper-mid, and 6G sub-THz communication systems.

SUK HWANGBO (Member, IEEE) received the B.S. degree in electronic engineering from Hanyang University, Seoul, South Korea, in 2023, and the M.S. degree from Seoul National University, Seoul, in 2025. He is currently with Wireless Semiconductor Division, Broadcom, Seoul, as a Hardware Engineer. His current research interests include the design of microwave integrated circuits for mobile use.

JUNGSUEK OH (Student Member, IEEE) received the B.S. and M.S. degrees from Seoul National University, South Korea, in 2002 and 2007, respectively, and the Ph.D. degree from the University of Michigan at Ann Arbor in 2012. From 2007 to 2008, he was with Korea Telecom as a Hardware Research Engineer, working on the development of flexible RF devices. In 2012, he was a Postdoctoral Research Fellow with the Radiation Laboratory, University of Michigan. From 2013 to 2014, he was a Staff RF Engineer with Samsung Research America, Dallas, working as a project leader for the 5G/millimeter-wave antenna system. From 2015 to 2018, he was a Faculty Member of the Department of Electronic Engineering, Inha University, South Korea. He is currently an Associate Professor with the School of Electrical and Computer Engineering, Seoul National University. He has published more than 50 technical journal and conference papers His research areas include mmWave beam focusing/shaping techniques, antenna miniaturization for integrated systems, and radio propagation modeling for indoor scenarios. He is the recipient of the 2011 Rackham Predoctoral Fellowship Award at the University of Michigan. He has served as a Technical Reviewer for the IEEE TRANSACTIONS ON ANTENNAS AND PROPAGATION and IEEE ANTENNA AND WIRELESS PROPAGATION LETTERS. He has served as a TPC Member and as a Session Chair for the IEEE AP-S/USNC-URSI and ISAP.